SWEDISH DEFENCE
RESEARCH AGENCY

FOI-R--0316--SE
December 2001
ISSN 1650-1942

Scientific report

Michael Tulldahl

Underwater Laser Beam Profiles after Transmission through a Wavy Sea Surface

Sensor Technology
SE-581 11 Linköping

SWEDISH DEFENCE RESEARCH AGENCY

Sensor Technology
P.O. Box 1165
SE-581 11 Linköping

FOI-R--0316--SE

December 2001

ISSN 1650-1942

Scientific report

Michael Tulldahl

Underwater Laser Beam Profiles after Transmission through a Wavy Sea Surface

Issuing organization
FOI – Swedish Defence Research Agency
Sensor Technology
P.O. Box 1165
SE-581 11 Linköping

Report number, ISRN
FOI-R--0316--SE

Report type
Scientific report

Research area code
4. C4ISR

Month year
December 2001

Project no.
E3026

Customers code
5. Contracted Research

Sub area code
43 Underwater Surveillance Sensors

Author/s (editor/s)
Michael Tulldahl

Project manager
Fredrik Kullander

Approved by
Svante Ödman

Sponsoring agency
Swedish Armed Forces

Scientifically and technically responsible
Michael Tulldahl

Report title

Underwater Laser Beam Profiles after Transmission through a Wavy Sea Surface

Abstract (not more than 200 words)

The effects of surface waves on laser beam transmission through the sea surface are experimentally examined. The purpose is to obtain experimental data for validation of laser pulse propagation models. Such data require simultaneous measurements of the time and space variability of the air-sea interface. Two significant consequences of transmission through the sea surface are investigated: beam widths at different depths averaged over several surface wave periods, and surface wave focusing or defocusing quantified by the irradiance fluctuations as a fractional fluctuation (standard deviation divided by the mean). The irradiance fractional fluctuations show a near-surface maximum and decay with depth. A submerged screen, filmed by an underwater video camera, is used to measure the downwelling irradiance profiles. The laser beam diameter at the water surface is 42 cm, and irradiance profiles are measured from 1.2 m to 3 m depth. All measurements are performed with the laser beam directed vertically downwards. Transmission for off-nadir angles is not tested in this experiment and no polarization effects are measured. The measurements are made in calm winds, 1 m/s to 3 m/s. The surface waves are measured with a video camera, and the dominant seasurface wavelength is about 0.25 m.

Keywords
laser, lidar, sea surface waves, beam profiles, ocean optics

Further bibliographic information

Language English

ISSN 1650-1942

Pages 31 p.

Price acc. to pricelist

Security classification

Utgivare

Totalförsvarets Forskningsinstitut - FOI
Sensorteknik
Box 1165
581 11 Linköping

Rapportnummer, ISRN
FOI-R--0316--SE

Klassificering
Vetenskaplig rapport

Forskningsområde
4. Spaning och ledning

Månad, år
December 2001

Projektnummer
E3026

Verksamhetsgren
5. Uppdragsfinansierad verksamhet

Delområde
43 Undervattenssensorer

Författare/redaktör
Michael Tulldahl

Projektledare
Fredrik Kullander

Godkänd av
Svante Ödman

Uppdragsgivare/kundbeteckning
Försvarsmakten

Tekniskt och/eller vetenskapligt ansvarig
Michael Tulldahl

Rapportens titel (i översättning)

Laserstrålprofiler under vatten efter transmission genom vattenyta med vågor

Sammanfattning (högst 200 ord)

Rapporten redovisar mätningar av vattenytvågors inverkan på lasertransmission genom vattenytan. Syftet med arbetet är att ta fram data för validering av laserutbredningsmodeller, vilket kräver samtidig mätning av tid- och rumsvariationer av vattenytans form. Två karakteristiska effekter av transmissionen genom vattenytan undersöks: tidsmedelvärdet av laserstrålbredden som funktion av djupet, samt fokusering och defokusering av laserstrålen kvantifierad av den normerade fluktuationen av irradiansen (standardavvikelsen dividerat med medelvärdet). Den normerade fluktuationen har ett maximum nära vattenytan och avtar sedan monotont med ökande djup. Irradiansen mäts genom att en horisontell vit skärm under vattenytan filmas av en undervattensvideokamera. Laserstrålens diameter är 42 cm när den träffar vattenytan och strålprofiler mäts från 1.2 m till 3 m djup. Mätningarna genomförs med laserstrålen riktad lodrätt nedåt. Sneda infallsvinklar och polarisationseffekter undersöks inte i experimentet. Mätningarna genomförs i svag vind, 1 m/s till 3 m/s. Vattenytans form mäts med en videokamera och den dominerande våglängden hos vattenytvågorna är 0.25 m.

Nyckelord

laser, lidar, havsvågor, strålprofiler, undervattensoptik

Övriga bibliografiska uppgifter

Språk Engelska

ISSN 1650-1942

Antal sidor: 31 s.

Distribution enligt missiv

Pris: Enligt prislista

Sekretess

Contents

1 Introduction

The subject of irradiance fluctuations in the sea has been studied by a number of authors. Measurements of sunlight fluctuations and their interpretation in terms of surface wave structure have been reported by Fraser *et al.*[1] Early theoretical and experimental work was made by Snyder and Dera.[2] McLean and Freeman reported a theoretical work that includes estimations of downwelling irradiance from laser transmission.[3] The work by Kattawar and Adams[4] is an example of Monte Carlo simulations that take the polarization effects into account for transmission through the sea surface.

The purpose of the present work is to obtain experimental data for validation of laser pulse propagation models under development at our department. Data for accurate model validation requires simultaneous measurements of the time and space variability of the air-sea interface, which consequently are presented in this report. Data sets of laser irradiance below the sea surface together with complete sea surface data are today rarely found in the literature.

In this experimental work a 2 m × 2 m screen was deployed from a quay with the goal of determining the spatial and temporal downwelling irradiance profiles below the sea surface, from a laser beam above the sea surface. In this way the image of the downwelling irradiance projected on the screen could be captured with an underwater camera directed against the screen. The screen and the camera are shown in Figure 1. The laser source was a frequency doubled pulsed Nd:YAG, with 4 ns pulse length and 100 μJ per pulse at 532-nm wavelength. The beam diameter at the water surface was 42 cm. All the measurements were performed with the laser beam directed at nadir downwards. Transmission with off-nadir angles was not tested in this experiment and no polarization effects were measured. The measurements were made in a small harbor in the Swedish lake Vättern with calm winds, 1 m/s to 3 m/s. The water optical attenuation (total attenuation) was measured with a C-βeta instrument (Hobi-Labs) to 0.45 m^{-1}. The measurements were done in darkness.

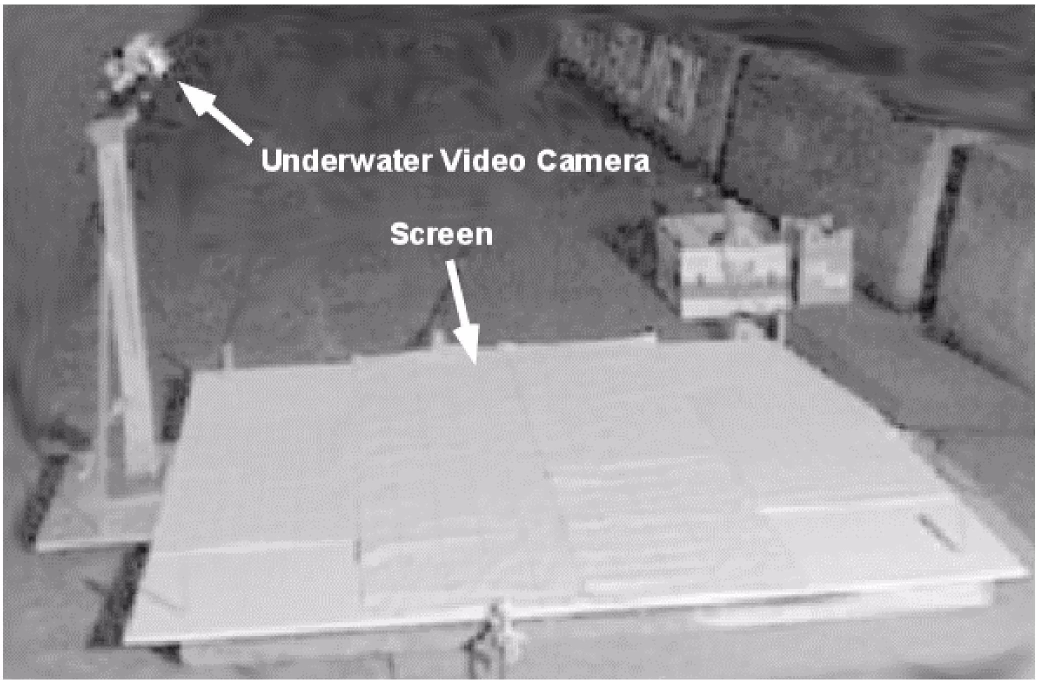

Figure 1. The beam profile screen with attached underwater video camera.

2 Measurements

The measurements were made in the harbor Hästholmen in the lake Vättern in September of 2001. The 2 m × 2 m screen was painted with white paint. The paint was dull, to avoid specular reflections from the screen. A Sony DCR-PC7E digital video camera was mounted inside an underwater housing and on the side of the screen as shown in Figure 1. The image of the downwelling irradiance projected on the screen was captured with the camera charge coupled device (CCD). The camera was equipped with a wide-angle objective; a bi-concave lens with focal length 50 mm. The entrance pupil of the camera was located 1 m above the screen plane. The camera focus was locked at the distance to the center of the screen, and the integration time (1/25 sec. per frame) and the aperture were locked at values for optimal use of the dynamical range of the CCD. The maximum measured irradiance was at 70 % – 80 % of the 256-level range of the CCD maximum intensity. The measurements, including the calibration measurements described in Section 3, were done in darkness. The screen depth was manually adjusted with steel rods fixed to the screen. The screen was balanced for slightly negative buoyancy, and the rods permitted the screen to be kept still during measurements, both vertically and horizontally. The rods were painted black to reduce reflected light from the rods.

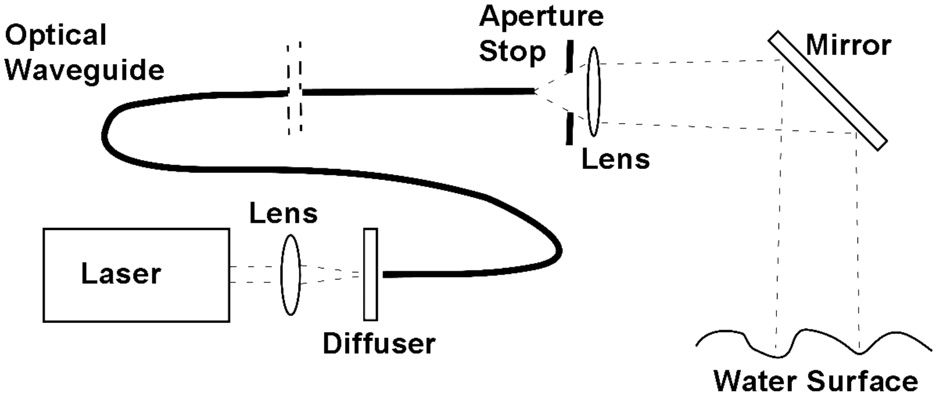

Figure 2. Schematic illustration of the laser transmitting system.

The laser source was a frequency doubled pulsed Nd:YAG, with 4 ns pulse length and the energy 100 μJ per pulse at 532-nm wavelength. A pulse repetition frequency of 4000 Hz was employed. Thus, the energy from 160 pulses was collected in each CCD-image. The laser light was led through an optical waveguide (a 1-mm diameter optical fiber) to the exit lens, where a beam full angle of 120 mrad was created with an aperture stop and a convex lens. The laser transmitting system is schematically illustrated in Figure 2. At the entrance of the waveguide a lens focused the beam onto the core of the fiber, and a diffuser was introduced between the lens and the fiber. The diffuser scattered the light, so the fiber modes were filled and a homogenous irradiance distribution in the exit beam was accomplished. The irradiance varied less than 5 % from the mean within 95 % of the exit beam diameter. From the exit lens, the beam was directed onto the water surface above the screen via a 45 cm × 45 cm mirror. The optical path length from the exit lens to the water surface was 3.5 m, and the circular beam at the water surface had a diameter of 42 cm. All the measurements were performed with the laser beam directed at nadir (vertically downwards). Transmission with off-nadir angles was not tested in the experiment.

3 Irradiance estimation

Calibrated values of downwelling irradiance could be obtained by reference measurements in laboratory, from which transformation functions from camera pixel intensity to downwelling irradiance reaching the screen were produced. The screen and the camera were used in the same setup as in the field experiment, see Figure 1 and Figure 2, with the exception that only one half of the screen was employed. Half of the screen was taken away to fit the equipment into the laboratory tank. One possible way to do calibration could have been to do a straight forward transformation from camera pixel intensity to downwelling irradiance for a point located on the center of the screen and use this function for all the positions on the screen. Our initial experimental evaluations showed however that different positions on the screen gave slightly different transformation functions. A more accurate method would be to generate functions at a limited number of positions, and then perform linear interpolation of the irradiance for points between these positions. We chose to generate transformation functions at nine positions on the screen, which was found to provide sufficient accuracy for our purpose. The locations of these positions were chosen so that they jointly covered the area corresponding to the measured beam profiles. Data for those positions were obtained by the laboratory measurements, where the laser beam was directed at six zones on the left half of the screen, see Figure 3.

With the laboratory measurements we were able to incorporate relevant factors into the transformation functions. Such factors include, for different positions on the screen: the screen-camera path length (attenuation and defocusing), and the angle between the camera and the screen normal. In the tank, filled with fresh water, the optical attenuation was measured with a C-βeta instrument (Hobi-Labs) and modified by adding small amounts of Maalox. In the laboratory measurements the water surface was flat. A laser beam with constant laser power and spot size was aimed at the six different zones on the screen, shown in Figure 3. For each zone, known relative irradiances were created from the laser beam blocked by different neutral density (ND) filters, and CCD images were recorded. The camera integration time and aperture were locked on the same level as in the field experiment.

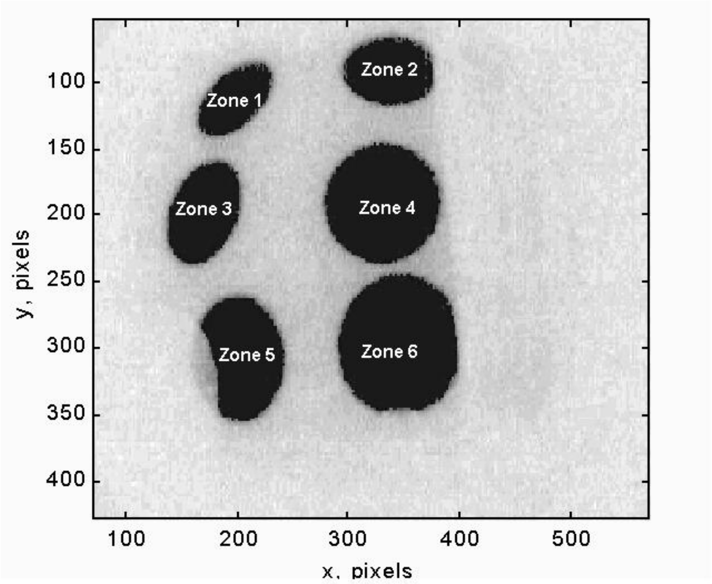

Figure 3. Illustration of the six zones used for generation of the transformation from pixel intensity values to calibrated irradiance.

Data from the laboratory measurements are shown in Figure 4. The figure also shows first-degree polynomial estimations, fitted to the measured data. For each zone, the CCD pixel intensity range is divided into three sections. The section limits are manually chosen and are given one polynomial for each of the sections. Additionally the standard deviations of the polynomial approximations are estimated with basis from the measured data. We use these standard deviations as error estimations for the irradiances calculated with the polynomials from the CCD pixel values.

To calculate the irradiance that hits a specific point on the screen, we calculate a distance-weighted average of the polynomial irradiance estimates from the nearest zones (1 to 6) to that specific point. We describe the procedure in detail by considering Figure 5, where the CCD image has been divided into four areas A to D. Points P1 to P6 are defined and marked with white dots in the respective zones 1 to 6. Additionally, mirror points P1b, P3b and P5b to points P1, P3 and P5 are defined.

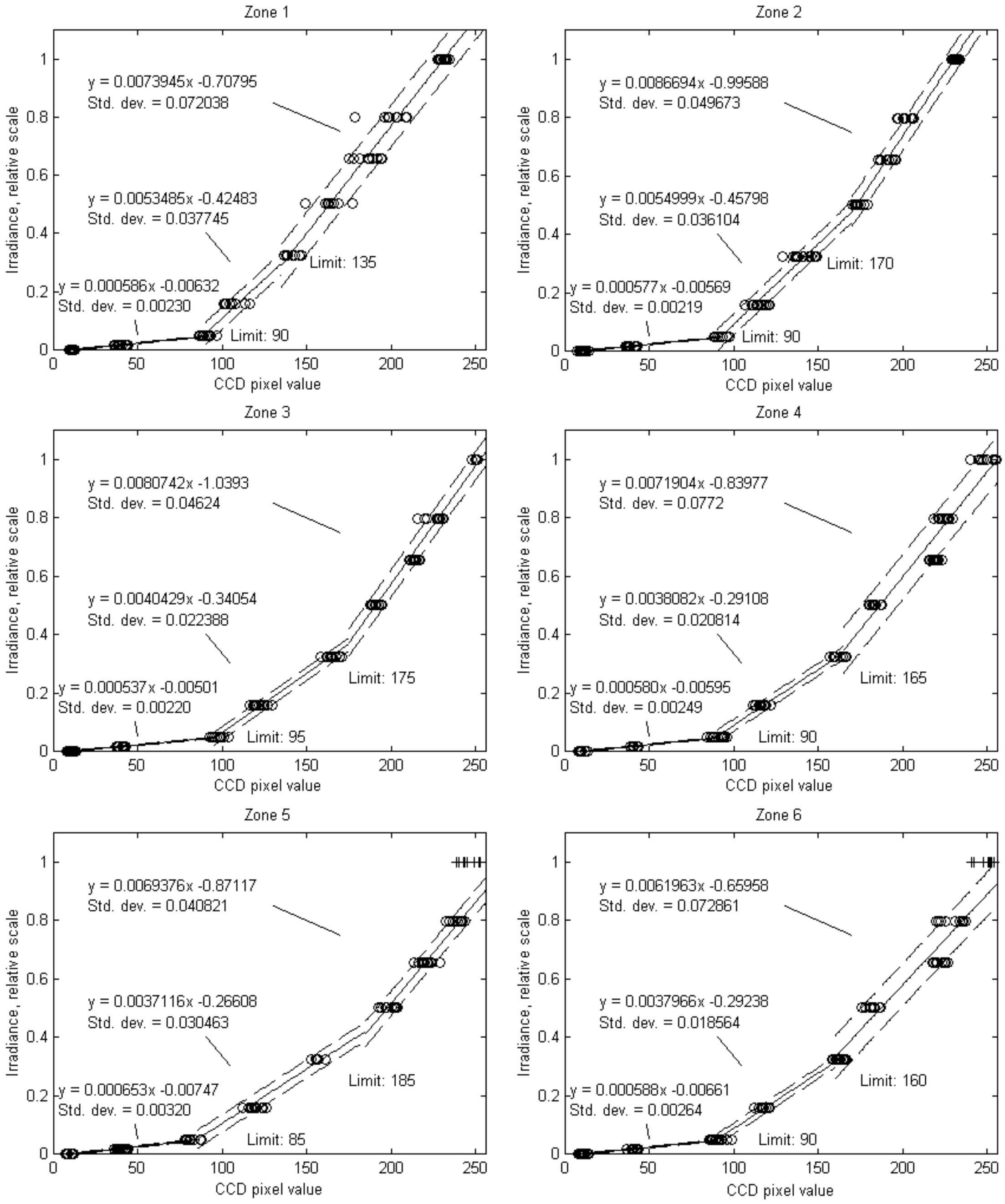

Figure 4. Transformation from CCD pixel intensity (*x*-axes) to irradiance (*y*-axes) in zones 1 to 6. Rings represent data for measured pixel intensities for known relative irradiances created from a laser beam blocked by neutral density filters. Solid lines show piecewise first-degree polynomial predictions fitted to the data. The dashed lines show the corresponding standard deviations for the error bounds. The errors are assumed to have normal distributions. The plus signs indicate that the data points have been excluded from the polynomial fitting, due to saturation of the CCD.

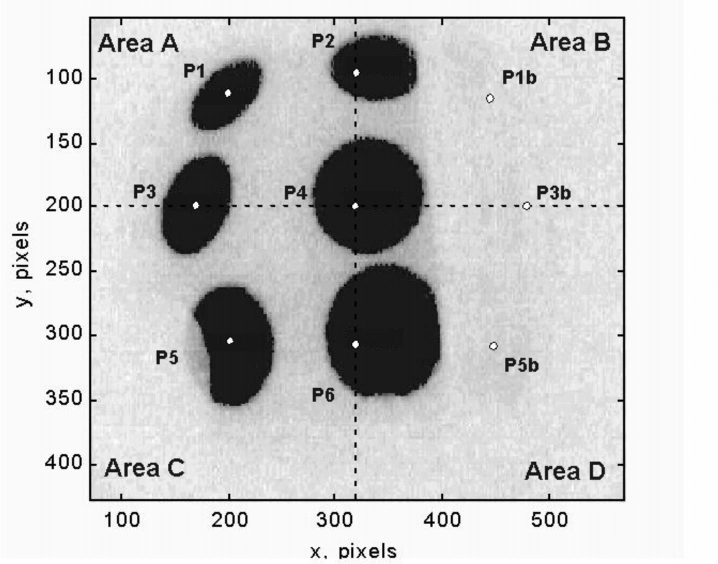

Figure 5. The CCD image has been divided into four areas A to D separated by dashed lines. Points P1 - P6, in white, are defined in the respective zones 1 - 6. In addition, mirror points P1b, P3b and P5b to points P1, P3 and P5 are defined.

If a specific point P is in Area A, we start by computing the distance-weighted average irradiance in the x-direction, relative to P1 and P2

$$\overline{E}_{12} = w_1 E_1 + w_2 E_2, \tag{1}$$

where E_1 and E_2 are the irradiances calculated from the polynomial models in Figure 4, for Zone 1 and Zone 2 respectively. The sum of w_1 and w_2 equals one, and their respective values are given by

$$w_1 = \frac{x_{P2} - x_P}{x_{P2} - x_{P1}}, \text{ and} \tag{2}$$

$$w_2 = \frac{x_P - x_{P1}}{x_{P2} - x_{P1}}, \tag{3}$$

where the variables x_{P1}, x_P, x_{P2} are the x-pixel coordinates for P1, P, and P2 respectively. However if $x_P < x_{P1}$, that is, if the specific point P is left of P1 we set

$$\overline{E}_{12} = E_1 .$$

Still considering the point P in Area A, we next compute the distance-weighted average irradiance in the x-direction, relative to P3 and P4

$$\overline{E}_{34} = w_3 E_3 + w_4 E_4 , \tag{4}$$

where E_3 and E_4 are the irradiances calculated from the polynomial models in Figure 4, and w_1 and w_2 are their respective weights given by

$$w_3 = \frac{x_{P4} - x_P}{x_{P4} - x_{P3}} \text{, and} \tag{5}$$

$$w_4 = \frac{x_P - x_{P3}}{x_{P4} - x_{P3}} . \tag{6}$$

The variables x_{P3}, x_{P4} are the x-pixel coordinates for P3, and P4 respectively. However, if $x_P < x_{P3}$ that is if the specific point P is left of P3 we set

$$\overline{E}_{34} = E_3 .$$

Finally, we compute the estimated irradiance in point P as the distance-weighted average of $\overline{E}_{12}$ and $\overline{E}_{34}$ in the y-direction, by

$$\overline{E}_P = w_{12} \overline{E}_{12} + w_{34} \overline{E}_{34} , \tag{7}$$

where w_1 and w_2 are given by

$$w_{12} = \frac{y_{34} - y_P}{y_{34} - y_{12}}, \text{ and} \tag{8}$$

$$w_{34} = \frac{y_P - y_{12}}{y_{34} - y_{12}}. \tag{9}$$

The coordinates $y_{34} = y_3 = y_4$, $y_{12} = (y_1 + y_2)/2$, and y_P are the y-pixel coordinates for P3, P4, for the mean of P1, P2 and for point P respectively. However, if $y_P < y_{12}$, that is if the specific point P is above y_{12}, we set

$$\overline{E}_p = \overline{E}_{12} .$$

The error estimate of the irradiance $\overline{E}_p$ in point P is calculated in a similar way to $\overline{E}_p$. Since $\overline{E}_p$ is a linear combination of E_1 to E_4, we can use the Eqs. (1)-(9), with the irradiance E changed to variance s^2 to obtain the error estimate of the irradiance $\overline{E}_p$ in point P. For example, from Eq. (1) we have the weighted average

$$s_{12}^{\ 2} = w_1 s_1^{\ 2} + w_2 s_2^{\ 2}, \tag{10}$$

of the estimated standard deviations s_1 and s_2 from Zone 1 and Zone 2 in Figure 4. Note in Figure 4 that, because of the piecewise polynomial approximations, the estimated standard deviation will increase in three steps with increasing pixel intensity. Similarly as for Eqs. (4) to (7), we write the variance for the error estimate of the irradiance $\overline{E}_p$ in point P

$$s_P^{\ 2} = w_{12} s_{12}^{\ 2} + w_{34} s_{34}^{\ 2}. \tag{11}$$

If the specific point P is located in areas B, C, or D in Figure 5, similar methods are used to estimate the irradiance $\overline{E}_p$ and the estimated variance $s_P^{\ 2}$.

4 Spatial distribution estimates

In conjunction with the field experiment a 10-cm grid was fixed onto the screen. An image of the grid from the underwater video camera is shown in Figure 6. The camera location relative to the screen and the wide-angle lens generate a spatial image distortion that demands a transformation of the images before they can be used for estimation of the spatial distributions of the downwelling irradiance. The calibration of a distorted image can be described in two steps:[5] first, the displacement between the origin of 3D-space of the screen and the camera coordinate system, which forms the external calibration parameters (3D-rotation and translation), and second the mapping between 3D-points in space and 2D-points on the camera image plane, which forms the internal camera calibration parameters (calibration of distortion caused e.g. by a wide-angle lens).

There are different kinds of calibration methods available.[5] The first kind of calibration method uses a calibration grid with feature points whose world 3D-coordinates are known. The calibration method finds the best camera external (rotation and translation) and internal (image aspect ratio, focal length, and possibly others) parameters that correspond to the position of these points in the image. A problem with this method occurs from the fact that there is a coupling between internal and external parameters that may result in high errors on the camera internal parameters. In our application however, this problem can be ignored because we do not need to describe the camera internal parameters separately. We will perform an image transform where the external and internal calibration parameters are combined. Another kind of method uses geometric invariants of the image, rather than known 3D-coordinates, like parallel lines or the image of a sphere. The last kind of calibration techniques is those that do not need any kind of known calibration points. These are also called auto-calibration methods, and a problem with these methods is that if all the parameters of the camera are unknown, they can be very unstable. Known camera motion helps however in getting more stable and accurate results. Since we easily can make use of a calibration grid, we use the first method with the modification that the external and internal calibration parameters are combined.

Let us consider the CCD image from the underwater camera, with the 10-cm grid fixed onto the screen, Figure 6. We will now describe our spatial calibration transform of the CCD image pixel coordinates to metric horizontal screen coordinates. The desired transform will calculate the spatial coordinates on the screen in meters (x_m, $y_{m,}$, z_m) from the camera pixel coordinates (x_{pxl}, y_{pxl}). In the following, the z_m-coordinate will be omitted, and we will always consider z_m to be equal to zero in the screen plane. We choose the metric coordinate system to have its origin in the center of the horizontal screen, which corresponds to the pixel coordinates $x_{pxl} \approx 330$ and $y_{pxl} \approx 220$. The pixel coordinates have the values

$$1 \le x_{pxl} \le 640, \text{ and } 1 \le y_{pxl} \le 480,$$

and the optical axis of the camera is in ($x_{pxl} = 320$, $y_{pxl} = 240$). To obtain the x_m-coordinate, we consider Figure 6 and realize the symmetry around the line $x_{pxl} = 320$ and write the following equation:

$$x_m = \left(x_{pxl} - 320\right)A + B \ , \tag{12}$$

where A is a positive scale factor which depends on both the x_{pxl} and y_{pxl} coordinates, and B is a constant (unit: meters) that moves the CCD-image of the metric y-axis to $x_m = 0$. The factor A of Eq. (12) takes into account the image distortion as a deformation of the image along the direction from a point called the center of distortion[5] to the considered image point. From a magnification of Figure 6 we obtain $B = -0.021$ m. We define

$$150 \le x_{pxl} \le 490 \qquad , \text{and} \quad 130 \le y_{pxl} \le 380,$$

to be the limiting conditions for the entirety of all the measured beam profiles, and approximate the scale factor A with the equation:

$$\hat{A} = \left|320 - x_{pxl}\right|^{\alpha_1} a_1 + \left|380 - y_{pxl}\right|^{\alpha_2} a_2 + \left[\left|320 - x_{pxl}\right| \times \left|380 - y_{pxl}\right|\right]^{\alpha_3} a_3 + a_4 , \tag{13}$$

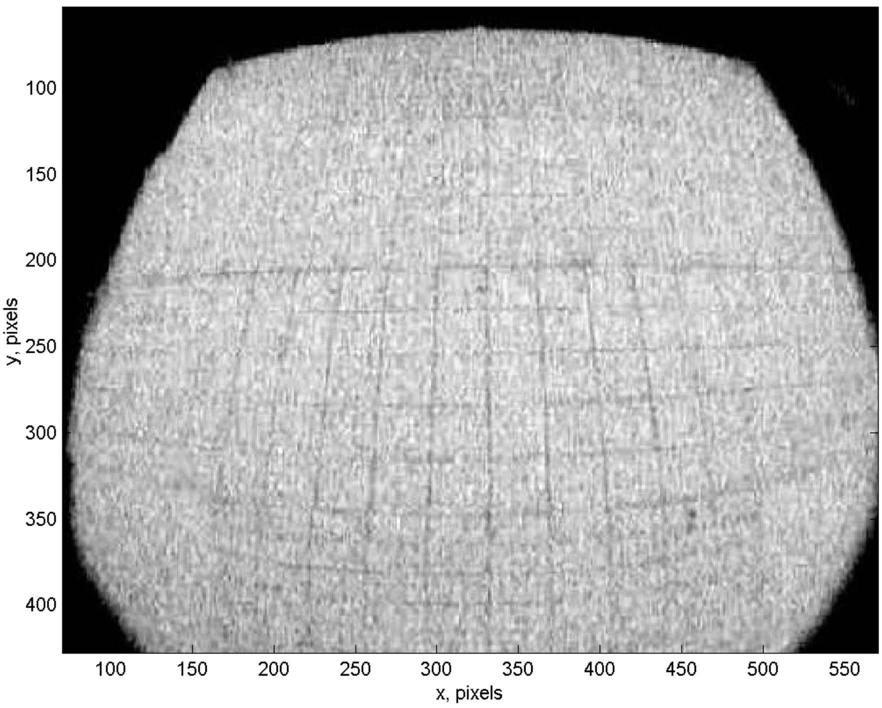

Figure 6. CCD image from the underwater camera with a 10-cm grid fixed on the screen. The camera and the screen are both below the water surface.

where $a_1,\ldots,a_4$ are real numbers and α_1, α_2, α_3 are real numbers > 0. Equation (13) describes the dependence of $\hat{A}$ on powers of the distances from the lines $x_{pxl} = 320$ and $y_{pxl} = 380$, and on the product of these distances. The constant $a_4 > 0$ is the initial scale factor in the point $x_{pxl} = 320$, $y_{pxl} = 380$. Since we use the external and internal camera calibration parameters combined, we use a somewhat different form for the parameter A than in Ref. 5. In that reference (other notation than "A" is used), the internal calibration parameters are decoupled from the external parameters, and factor A is mainly dependent on the distance from the center of the CCD-image. From Figure 6 we conclude that $\hat{A}$ is monotonically increasing with $|320 - x_{pxl}|$ and $|380 - y_{pxl}|$. Thus the factors a_1 and a_2 will have positive values. Initial transform evaluation showed that the third term on the right hand side of Eq. (13), i.e. the product of the distances from $x_{pxl} = 320$, $y_{pxl} = 380$, was necessary to obtain sufficient accuracy. We perform the estimation of $a_1,\ldots,a_4$ and α_1, α_2, α_3 in three steps.

First, we take five points along the line $y_{pxl} = 380$ and thus reduce the right hand side of Eq. (13) to contain only the first and last terms. For each of those five points $k = 1,..,5$ from the CCD-image, we calculate A_k with Eq. (12) and numerically perform least squares estimates of a_1 and a_4 for a set of α_1-values. For each α_1-value we find a_1 and a_4 that is of best fit in the sense of the least square (LS) method, i.e. such that

$$Q_{\alpha_1} = \sum_{k=1}^{5} (\hat{A}_k - A_k)^2 \bigg|_{y_{pxl}=380} \tag{14}$$

is minimized. Then we find α_1 such that Q_{α_1} is minimized, to obtain the complete LS estimate of a_1, a_4 and α_1.

In the second step we take five points along the line $x_{pxl} = 320$ and thus reduce Eq. (13) to contain only the second and last terms on the right hand side of the equation. Similarly to the first step we obtain the estimates for a_2 and α_2.

In the third step we take five points along a diagonal line in the CCD-image (Figure 6) that starts from $x_{pxl} = 320$, $y_{pxl} = 380$ and terminates at $x_{pxl} = 490$, $y_{pxl} = 380$, i.e. within the limited area for the entirety of all the measured beam profiles. The LS-estimates for a_3 and α_3 is obtained by inserting the estimates of a_1, α_1, a_2, α_2, a_4 and Eq. (13) into Eq. (14).

To obtain the y_m-coordinate, we consider Figure 6 and realize that the line $y_{pxl} = 250$ should be transformed onto a straight line in the metric coordinate system and write the following equation:

$$y_m = (250 - y_{pxl})C + D \ , \qquad y_{pxl} \le 250 \tag{15}$$

where C is a positive scale factor which depends on both the x_{pxl} and y_{pxl} coordinates, and D is a constant (unit: meters) that moves the CCD-image of the metric x-axis to $y_m = 0$. In contrast to the x-coordinate transform, we do not have symmetry, so an additional equation valid for $y_{pxl} > 250$ will be given later in the text. From a magnification of Figure 6 we obtain D = -0.17 m. In the same way as for the x coordinate we approximate the scale factor C to the equation:

$$\hat{C} = \left|320 - x_{pxl}\right|^{\gamma_1} c_1 + \left|250 - y_{pxl}\right|^{\gamma_2} c_2 + \left[\left|320 - x_{pxl}\right| \times \left|250 - y_{pxl}\right|\right]^{\gamma_3} c_3 + c_4, \qquad (16)$$

where $c_1,\ldots,c_4$ are real numbers and γ_1, γ_2, γ_3 are real numbers > 0. Equation (16) describes the dependence of $\hat{C}$ on powers of the distances from the lines x_{pxl} = 320 and y_{pxl} = 250, and on the product of these distances. The constant $c_4 > 0$ is the initial scale factor in the point x_{pxl} = 320, y_{pxl} = 250. From Figure 6 we conclude that $\hat{C}$ is monotonically increasing with $|320 - x_{pxl}|$ and $|380 - y_{pxl}|$. Thus the factors c_1 and c_2 will have positive values. We perform the estimation of $c_1,\ldots,c_4$ and c_1, c_2, c_3 in three steps as we did with the parameters in Eq. (13). To obtain the y_m-coordinate, for $y_{pxl} > 250$ we also have that the line y_{pxl} = 250 should be transformed onto a straight line in the metric coordinate system and thus write

$$y_m = \left(250 - y_{pxl}\right)E + D\ , \qquad y_{pxl} > 250, \qquad (17)$$

where E is a positive scale factor, which depends on both the x_{pxl} and y_{pxl} coordinates, and D is the same constant as in Eq. (15). In a similar way as for $y_{pxl} \leq 250$ we approximate the scale factor E with the equation:

$$\hat{E} = \left|320 - x_{pxl}\right|^{\varepsilon_1} e_1 + \left|250 - y_{pxl}\right|^{\varepsilon_2} e_2 + \left[\left|320 - x_{pxl}\right| \times \left|250 - y_{pxl}\right|\right]^{\varepsilon_3} e_3 + e_4, \qquad (18)$$

where $e_1,\ldots,e_4$ are real numbers and ε_1, ε_2, ε_3 are real numbers > 0. These parameters are estimated with the LS-method, in the same way as the parameters in Eqs. (13) and (16).

An example of the spatial transform described by Eqs. (12) - (18) of a CCD-image in Figure 7 is shown in Figure 8. For clarity, the grid-line contrasts are manually improved in Figure 7.

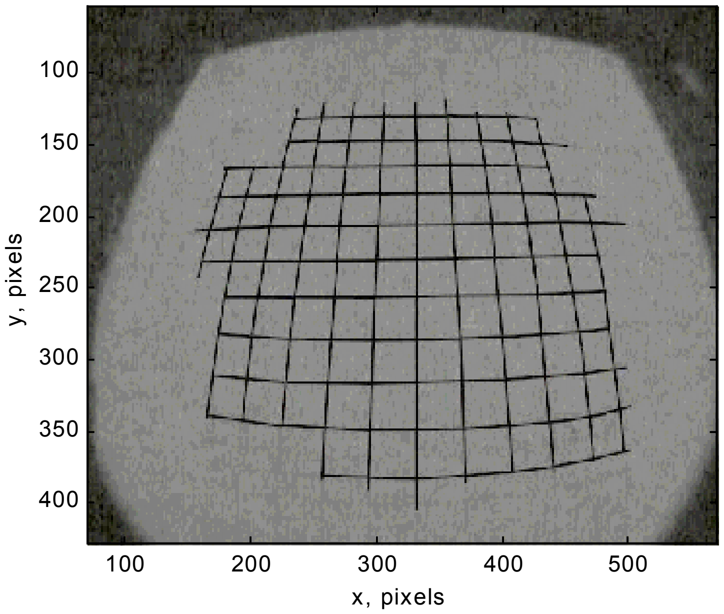

Figure 7. CCD image from the underwater camera with a 10-cm grid fixed on the screen. The grid lines in the center of the screen are manually augmented for better visibility.

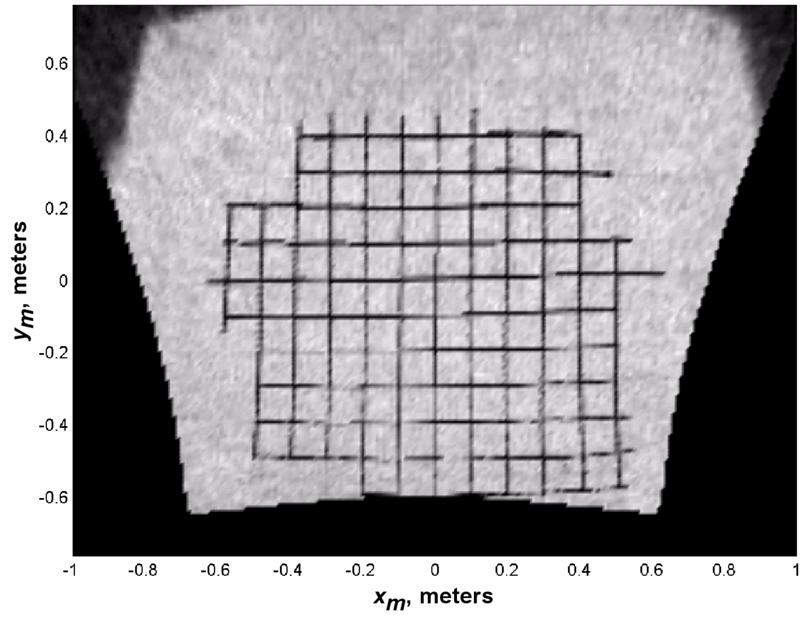

Figure 8. Spatially corrected image of Figure 7.

4.1 Error analysis

The accuracy in the transformation of coordinates to meters x_m, (and similarly for y_m), can be theoretically estimated by using Eq. (13), its parameters and a set of points from the CCD-image with calculated A_k -values. The estimated variance of $\hat{A}$ with respect to A is then given by

$$s_A{}^2 = \frac{1}{N-1}\sum_{k=1}^{N}(\hat{A}_k - A_k)^2 , \tag{19}$$

where N is the number of points taken from the CCD-image. For simplicity, we assume that the estimation of $\hat{A}$ has a normal distributed error around A, and thus that the estimate of the x_m-coordinate

$$\hat{x}_m = (x_{pxl} - 320)\hat{A} + B \tag{20}$$

has a normal distributed error around x_m with estimated variance

$$s_x{}^2 = (x_{pxl} - 320)^2 s_A{}^2 . \tag{21}$$

The theoretical error will increase with the distance from the line $x_{pxl} = 320$. The error estimates for $y_{pxl} \leq 250$ and $y_{pxl} > 250$ are calculated in a similar way. The calculated maximum standard deviations s_x from Eqs. (19)-(21), and similarly s_y, are shown in Table 1 together with the measured maximum errors from Figure 8 that occur at the border of the limited area for the measured beam profiles ($150 \leq x_{pxl} \leq 490$, and $130 \leq y_{pxl} \leq 380$). Another measure of the error of the spatial estimate is the relative error. In a magnification of Figure 8, we measured the relative errors in the x- and y-directions along a distance of 10 cm. The maximum relative errors along 10 cm was estimated to 0.5 cm, or 5 %, in both x- and y-directions as marked in the right column in Table 1.

Table 1. Calculated and measured errors of length scales for the spatially corrected CCD images.

	Calculated maximum standard deviation	Measured maximum error	Measured maximum relative error
$\hat{x}_m$	0.96 cm	1.5 cm	5 %
$\hat{y}_m$	0.45 cm	1.0 cm	5 %

4.2 Completing the irradiance and spatial estimates

The complete procedure for irradiance and spatial transforms of a CCD image, including error estimations, is done by first applying irradiance transform described in Section 3 on the all pixels in the image. We then create a grid for the spatially corrected image with 1-cm resolutions in both the x- and y-directions, where we insert the result from the spatial transform described in Section 4.

When the spatial transform is executed, several irradiance values E_P from pixels P will end up in the same cm grid square. All these values will be used to calculate an average irradiance E in the grid square

$$E = \frac{1}{N}\sum_{P=1}^{N} E_P \,, \tag{22}$$

where N is the number of pixel values in the grid square. From the irradiance transform we have for each pixel irradiance value, also an error variance value. Those variances s_p^2 are used to calculate the variance s^2 of the irradiance E

$$s^2 = \frac{1}{N}\sum_{P=1}^{N} s_P{}^2 \tag{23}$$

in each grid square. The number of pixels per grid square depend on the spatial scale factors and vary between 2 and 12 over the valid area for the spatial transform. The smallest number of pixels per grid square are at points on the screen that are far from the camera, i.e. to the right in Figure 1.

5 Wavelength and waveheight spectra

Fluctuations in the underwater light field just below the sea surface are dominated by the time and space variability of the air-sea interface. This dependence is manifested primarily in the sea-surface slope but in some cases may include other sea surface descriptors. According to Walker,[6] the underwater irradiance depends on the surface curvature and whitecap radiometry. The whitecap radiometry is sensitive to the wave breaking, generally attributed to excessive local vertical accelerations. In our experiment neither whitecaps nor wave breaking were observed, due to the low wind speed and the sheltered harbor environment, see Figure 9. The wind speed was measured with a cup anemometer, to 2-3 m/s at 4 m above the water surface, and to 0.5-1.5 m/s at 1 m above the water surface.

Hydrodynamic theory suggests that the surface wave spectrum naturally divides into subranges that are dominated by gravity forces (gravity waves), surface-tension forces (capillary waves or ripples), and viscous dissipation. In an equilibrium sea the spectral density peak is nominally at a point where the phase speed of longest wave matches the wind speed. At a surface wave frequency of about 13 Hz corresponding to a water surface wavelength of 0.017 m, gravitational and surface tension restoring forces become equal and the spectrum transitions between gravity and capillary waves.[6] Spectral cut-off is usually attributed to viscous effects, which become important at surface wave frequencies on the order of 10^2 - 10^3 Hz. Measurements of small scale waves require an instrumentation of high spatial resolution and short time response. In our experiment we measured the surface waves with a video camera with a frame rate of 25 Hz. Consequently the temporal resolution permitted the gravity waves down to the transition wavelength between gravity and capillary waves to be measured. A ruler was held along the wind direction, just above the water surface. With the video camera optical axis perpendicular to the ruler, the wave motion was recorded. In the video frame captures, the distance from the ruler to the water surface was measured manually. In Figure 10, examples of three water surface wave profiles are shown. The peak to peak wave height is approximately 2 cm and the dominant wavelength is about 0.25 m. The camera conveyed a spatial resolution of 1 mm of the surface waves. The estimated maximum errors for the measured wave elevation and the along wind distance are both 1 mm. The spatial resolution permitted measurements of

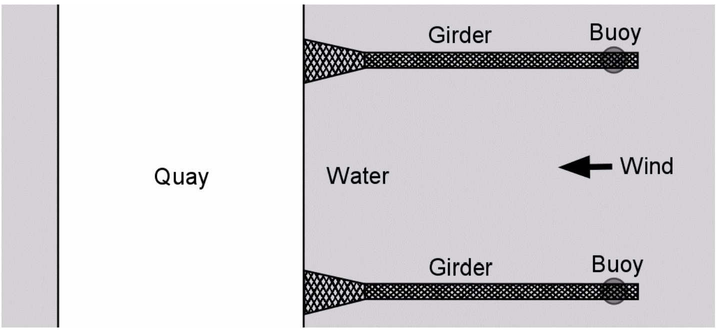

Figure 9. Schematic top-view of the measurement situation. The quay height above the water surface is 60 cm. The measurements of surface waves and of underwater beam profiles were done between the two girders.

surface waves approximately down to wavelengths of 0.04 m corresponding to a spatial frequency of 25 cycles/m, where their small wave amplitude on the order of millimeters limited measurements of shorter wavelengths. In summary, a maximum surface wave spatial frequency of about 25 cycles/m was measured taking both the temporal and spatial resolutions into account.

Because of the many uncertainties surrounding the non-linear surface wave physics, statistical models used for engineering studies such as radiometry and radar scattering are typically hybrids that combine semiempirical spectral models intended for an equilibrium sea with well defined linear random variable theory. The sea surface statistical concepts employed by authors, for example Mobley[7] and Stolte,[8] include measures such as the sea surface elevation spectral density and the frequency spectral density. The frequency spectral density is most common in the literature. The transformation between these spectral representations requires knowledge of the dispersion relation for the sea surface waves, and the directionality of the spectrum.

The water surface measurements presented in this report are given as the power spectral density of the surface elevation for a spectrum of water surface wavelengths. An averaged periodogram of ten water surface wave profiles is shown in Figure 11. The ten water surface profiles were collected with a time interval of 0.2 s between each profile. We can note the peak at the spatial frequency 4 cycles/m corresponding to the wavelength 0.25 m, which relates to the dominant wavelength of about 0.25 m in Figure 10. The periodogram was calculated as the mean of the normed absolute

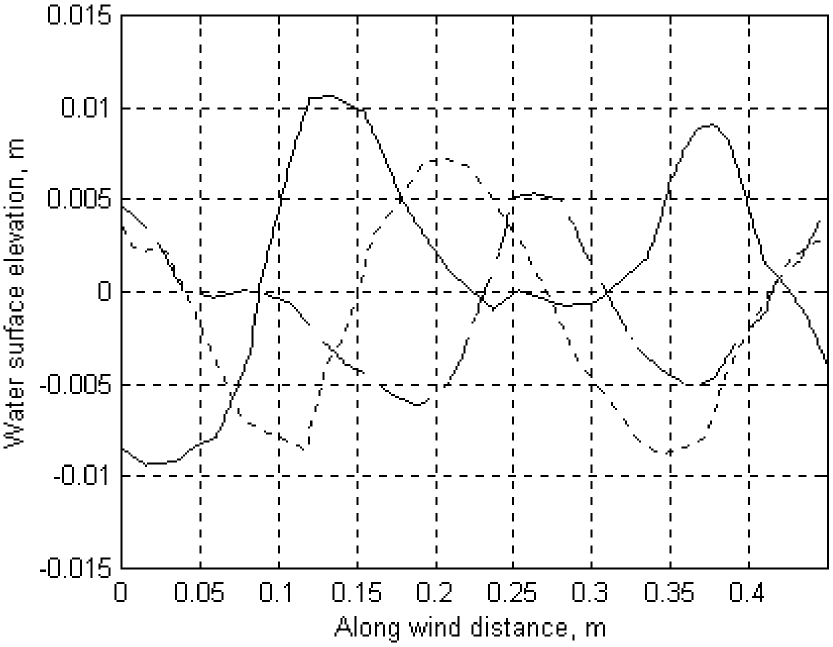

Figure 10. Example of three water surface wave profiles measured in the along-wind direction. The dominant wavelength is approximately 0.25 m and the maximum wave amplitude is about 1.1 cm.

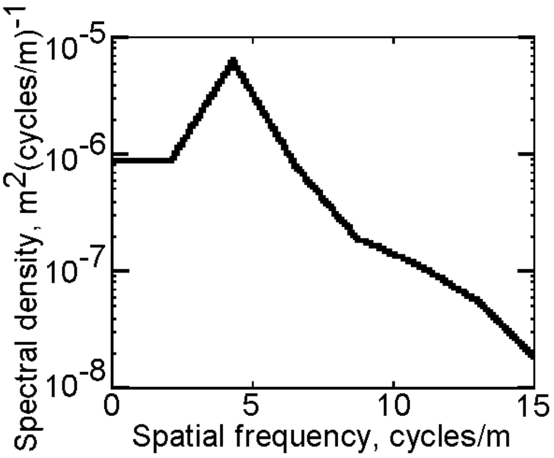

Figure 11. Average spectral density of ten along wind water surface wave profiles. The spectral peak is at a corresponding wavelength of 0.25 m, cf. Figure 10.

square of the discrete Fourier transforms of the water surface wave profiles. To contain the energy for negative frequencies that are not included in Figure 11, the spectral density values have been multiplied by two.

6 Results and discussion

Laser beam profile data were acquired at depths ranging from 1.2 m to 3 m below the water surface. Measurements of the irradiance profiles are exemplified in Figure 12. The images in this figure have been corrected according to the methods described in Sections 3 and 4 in this report. Our measurements exhibit the same non-linearity of the amplitude peaks as noted by McLean and Freeman.[3] They compare their simulations with calculations of irradiance below a single sinusoidal wave of wavelength λ with the focal length z of the cylindrical lens

$$z = \left(\frac{n}{n-1}\right)\left(\frac{1}{ak}\right)\frac{\lambda}{2\pi} \approx \frac{0.64}{ak}\lambda, \tag{24}$$

where n is the index of refraction of seawater (1.333) and ak is the non-dimensional wave steepness. A typical steepness is of the order of 0.05 to 0.2. Thus, the focusing depth is of the order of 3 to 12 times the surface wavelength. In our experiment the surface wave spectrum had a peak at about 0.25-m wavelength, so the maximum wave influence is expected at depths from approximately 0.75 m to 3 m. The influence of focusing is reduced at great depths because of the combined effects of decreasing curvature spectral energy and increased blurring caused by multiple scattering.

Figure 13 shows cross wind and along wind beam widths (full width at half of maximum - FWHM) at different depths averaged over 100 frames (4 seconds). The error estimates of the measured data are obtained by averaging the estimated variance in each pixel, see Section 4.2, over all 100 frames. In the same figure we also show the theoretical full beam width of a transmitted, homogeneous beam through a flat sea surface and unperturbed by scattering in water. Note that the homogeneous theoretical beam is given at its full width, so it can naturally be wider than the FWHM of the measured beam. The measured beam cross-section has obviously tails that go outside the FWHM. As one could expect, the along wind beam width generally is larger than the cross wind beam width.

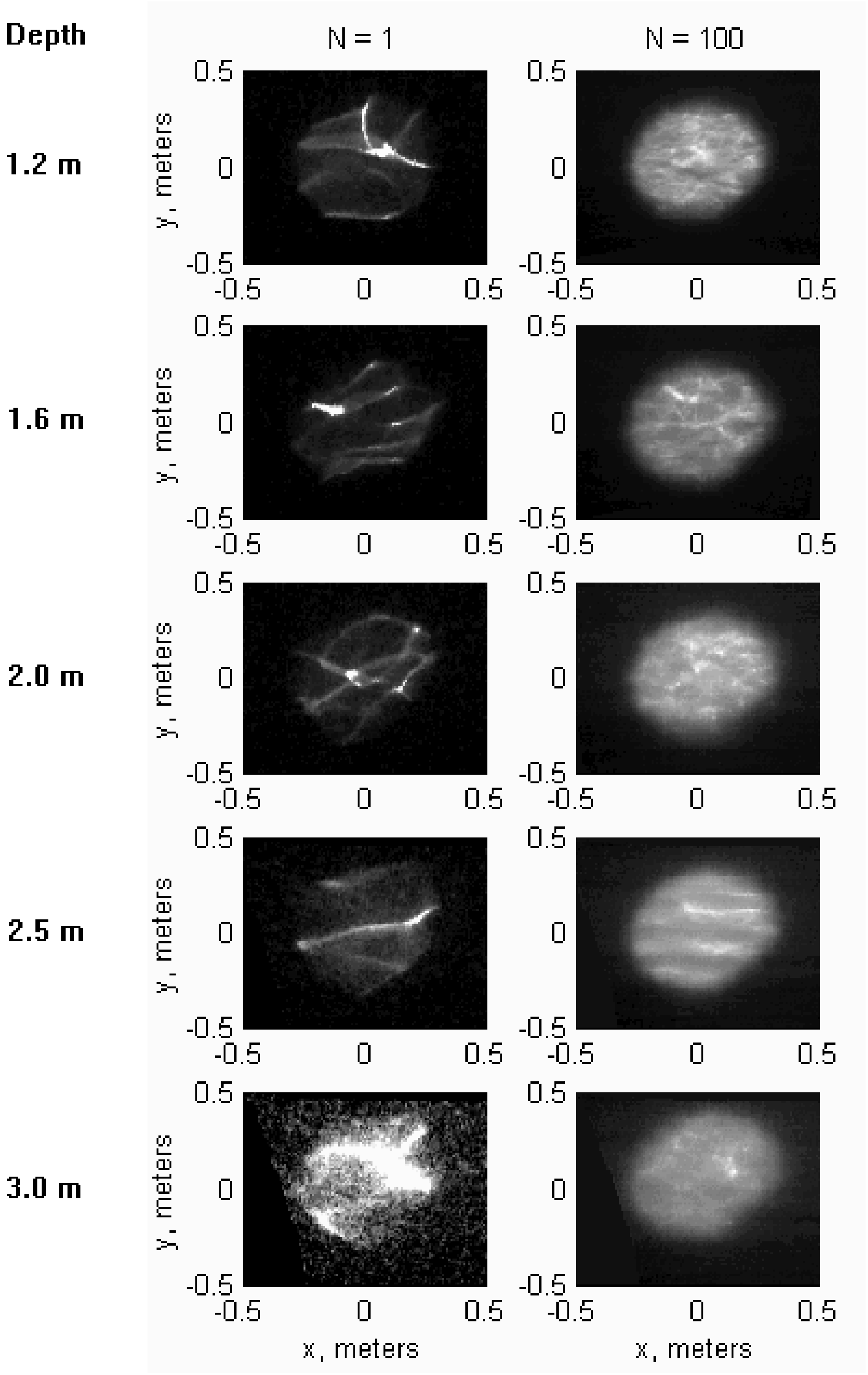

Figure 12. Examples of measured irradiance profiles at depths from 1.2 m to 3 m. To the left, samples from one frame (1/25 second), and to the right the mean irradiance profiles of 100 frames (4 seconds). The gray level of each image is adjusted to be white at 100 % relative irradiance for N = 100, and 25 % for N = 1. The same gray level thus represents four times higher irradiance in the left image than in the right image at each depth.

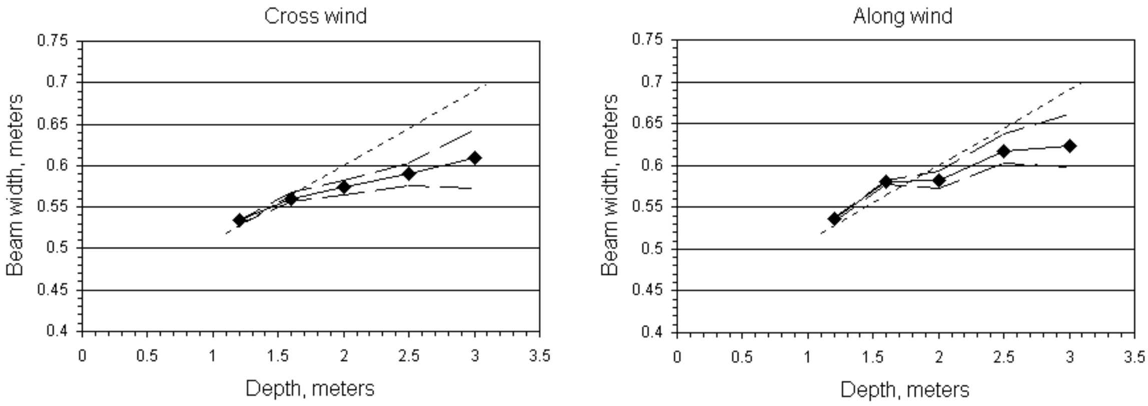

(a) (b)

Figure 13. Measured cross wind and along wind beam widths averaged over 100 frames (4 seconds) for depths 1.2 m to 3 m (solid lines) together with corresponding standard deviation for the estimated measurement errors (dashed). The dotted lines show the theoretical full beam width of the transmitted, homogeneous beam through a flat sea surface and unaffected by scattering in water. The measured beam widths are taken as the full width at half of maximum irradiance (FWHM).

Early measurements of surface wave focusing or defocusing quantified the irradiance fluctuations as a fractional fluctuation (standard deviation divided by the mean) σ_d / μ_d. In Figure 14, we compare the fractional fluctuations from our experiment with experimental data from Fraser *et al.*[1] and with theoretical data from McLean and Freeman.[3] The water types in those studies were relatively clear: Jerlov II type, with a diffuse attenuation coefficient of about 0.1 m^{-1}. The water type in our experiment had a total attenuation coefficient of 0.45 m^{-1}, which approximately corresponds to a diffuse attenuation coefficient of 0.16 m^{-1} according to Steinvall *et al.*[9] In Figure 14, our measured fractional fluctuations are higher than the compared data, but they qualitatively show the near-surface maximum and the decay with depth. A direct quantitative comparison is difficult because the illumination and wave conditions were somewhat different. The sun angle from nadir was 23° in the experiment by Fraser et al. The difference between the sun as a light source, and as in our experiment, a spatially limited laser beam at a distance (3.5 m) from the surface and could influence the results.

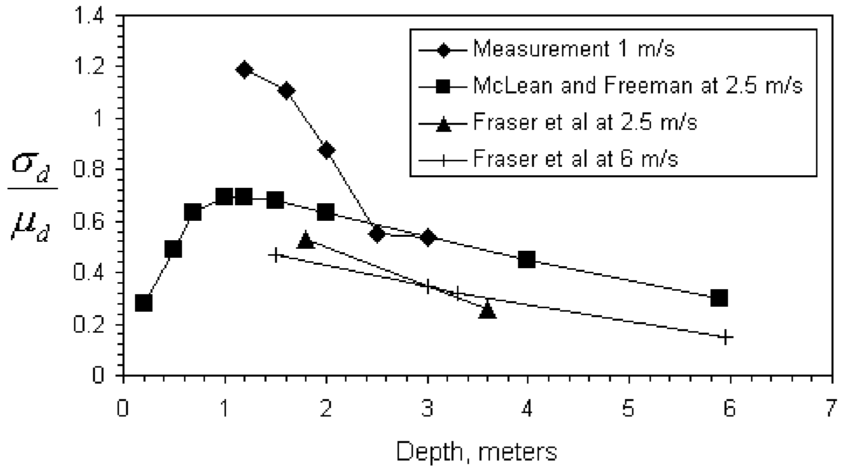

Figure 14. Fractional fluctuations of downwelling irradiance. Our measured data (measurement 1 m/s) are taken at a square of 10 cm × 10 cm at the center of the beam and the sample size is 100 frames.

7 Conclusions and future work

Spatial and temporal irradiance profiles below the sea surface was measured with a screen filmed by an underwater video camera. This measurement method allowed irradiance temporal and spatial resolutions of approximately 1/25 second and 0.5 cm respectively. The intensity dynamical range of the video camera limited our measurements to a maximum screen depth of about 3-m. If larger depths would be needed, it could be attained by increasing the laser power or decreasing the beam diameter. Our results on irradiance fluctuations qualitatively agree with published data. Considering solar downward irradiance fluctuations in seawater, the largest focusing effects are to be expected at high solar elevation and at wind speeds less than 5 m/s, which could be one explanation for the high irradiance fractional fluctuations we obtained in our measurements.[7]

The results from the work described in this report will be used for validation of a computer model, which primarily is constructed for simulation of an airborne laser depth sounding system. More precisely, the subject of the simulations is the effect of surface waves on the detection of small objects on the sea bottom. In an earlier simulation model, we treated the downward irradiance was as a sea surface slope average quantity.[10] In the upcoming model for laser transmission through the sea surface, we use a gravity wave spectrum to generate a random sea surface of triangular gravity wave facets. Then each of those facets is covered with a surface of capillary waves. The procedure has been described by Mobley.[7] In the validation of our computer model we will also use experimental data from the airborne laser depth sounder *Hawk Eye*.[9, 11] which allow comparisons of the time-resolved waveforms received from each transmitted and reflected laser *pulse*. The data from the work described in this report will allow *beam* propagation comparisons, with a detailed view of the irradiance distribution within the laser beam.

8 References

---

[1] A. B. Fraser, R. E. Walker, and F. C. Jurgens, "Spatial and temporal correlation of underwater sunlight fluctuations in the sea," *IEEE Journal of Oceanic Engineering,* vol. OE 5, no. 3, pp.195-198, 1980.

[2] R. L. Snyder and J. Dera, "Wave-induced light field fluctuations in the sea," *IEEE Journal of the Optical Society of America*, vol. 60, no. 1, pp. 1072-1078, 1970.

[3] J. W. McLean and J. D. Freeman, "Effects of ocean waves on airborne lidar imaging," *Applied Optics*, vol. 35, no. 18, pp. 3261-3269, 1996.

[4] G. W. Kattawar and C. N. Adams, "Errors in radiance calculations induced by using scalar rather than Stokes vector theory in a realistic atmosphere-ocean system," in *Proc. Ocean Optics X Conf.*, Orlando, USA: SPIE vol. 1302, 1990, pp. 2-12.

[5] F. Devernay and O. Faugeras, "Automatic calibration and removal of distortion from scenes of structured environments," in *Proc. Investigative and Trial Image Processing Conf.*, San Diego, California: SPIE vol. 2567, 1995, pp. 62-72.

[6] R. E. Walker, *Marine light field statistics*. John Wiley & Sons, Inc., New York, 1994.

[7] C. D. Mobley, *Light and Water*. Academic Press, San Diego, 1994.

[8] S. Stolte, "Short-Wave Measurements by a Fixed Tower-Based and a Drifting Buoy System," *IEEE Journal of Oceanic Engineering,* vol. 19, no. 1, pp. 10-22, 1994.

[9] K. O. Steinvall, K. R. Koppari, and U. C. M. Karlsson, "Airborne Laser Depth Sounding. System Aspects and Performance," in *Proc. Ocean Optics XII Conf.*, Bergen, Norway: SPIE vol. 2258, 1994, pp. 392-412.

[10] H. M. Tulldahl and K. O. Steinvall, "Analytical waveform generation from small objects in lidar bathymetry," *Applied Optics*, vol. 38, no. 18, pp. 1021-1039, 1999.

[11] K. O. Steinvall, K. R. Koppari, U. Lejdebrink *et al.*, "Depth Sounding Lidar-Performance and Models," in *Proc. Laser Radar Technology and Applications Conf.*, Orlando, Florida: SPIE vol. 2748, 1996, pp. 18-38.